4D-XCT monitoring of void formation in thick methacrylic composites produced by infusion

Q1 Q2

The corrections made in this section will be reviewed and approved by a journal production editor.

Sarah F. Gayot[a,b,*], sarah.gayot@uclouvain.be, Jeroen Soete[c], Johan Vanhulst[c], Pierre Gérard[d], Thomas Pardoen[a,e]

[a]~~Institute of Mechanics, Materials and Civil engineering (iMMC), UCLouvain B-1348 Louvain-la-Neuve, Belgium~~Institute of Mechanics, Materials and Civil engineering (iMMC), UCLouvain, B-1348 Louvain-la-Neuve, Belgium

[b]~~Institute of Condensed Matter and Nanosciences (IMCN), UCLouvain B-1348 Louvain-la-Neuve, Belgium~~Institute of Condensed Matter and Nanosciences (IMCN), UCLouvain, B-1348 Louvain-la-Neuve, Belgium

[c]~~Department of Materials Engineering, KU Leuven, Kasteelpark Arenberg 44 3001 Leuven, Belgium~~Department of Materials Engineering, KU Leuven, Kasteelpark Arenberg 44, B-3001 Leuven, Belgium

[d]~~Groupement de Recherche de Lacq, Arkema, RD 817, BP 34 64170 Lacq, France~~Groupement de Recherche de Lacq, Arkema, RD 817, BP 34, 64170 Lacq, France

[e]~~WEL Research Institute, avenue Pasteur 6 1300 Wavre, Belgium~~WEL Research Institute, avenue Pasteur 6, B-1300 Wavre, Belgium

*Corresponding author.

[Instruction: In the affiliation section, I only added commas and put a "B" in front of the Belgian post codes which did not have any.]

Abstract

Void formation in fibre-reinforced polymer composites processed by liquid moulding is a persistent issue in composite research and development. Not only may several void formation mechanisms come into play, but these defects can also accumulate and grow over the course of the manufacturing process. Mitigation methods can be applied once the underlying causes of voiding are identified, which is impossible through post-mortem characterisation. Here, void formation is dynamically monitored in miniaturised glass fibre-reinforced thermoplastic polymer composite samples manufactured by vacuum infusion and in-situ polymerisation, using laboratory-based X-ray computed tomography (XCT). The method allows the characterisation of the evolution of void patterns as the resin polymerises and cools down within the fibre preform. With a time resolution of 2 min and a voxel size close to 20 μm, this first-of-a-kind XCT experiment provides insights into the evolution of the void volume fraction, void size and location. The root causes leading to void formation in the system of interest were successfully identified as a combination of flow-related air entrapment during preform filling and, mostly, of chemical shrinkage of the matrix upon polymerisation. Additionally, thermal shrinkage during the cooling of the preform results in a slight decrease in the final void volume fraction.

Keywords:

Polymer matrix composites, Porosity, Microtomography, Processing, Liquid composite moulding

Abbreviations

FOV Field of view
LM Liquid moulding
LT Local thickness
MMA Methyl methacrylate
PMMA Polymethyl methacrylate
PVC Polyvinyl chloride
XCT X-ray computed tomography

1 Introduction

Fibre-reinforced polymer composites produced by liquid moulding processes generally contain voids, which can be detrimental to the mechanical properties of the structural components. While the formation of porosity cannot be entirely avoided, mitigation actions can be applied to control the main sources of void formation. These sources include incomplete resin degassing and void entrapment during mould filling, volatilisation of resin components (or polymerisation by-products) as well as chemical shrinkage during in-situ curing, and thermal shrinkage upon cooling [1–5]. The development of anti-void strategies implies a deep understanding of the root causes of the mechanisms involved in void formation for a given manufacturing process. Various characterisation methods exist for the post-mortem analysis of porosity in composite materials [6], such as X-ray computed tomography (XCT) [5,7], microscopy of polished cross-sections, thermography [8], or ultrasonic inspection [9]. However, the identification of the fundamental origins/sources of porosity remains elusive. When several mechanisms are involved in the process of void nucleation, growth and transport, post-mortem methods are unable to separate the contribution of each phenomenon and to reconstruct the timeline of events.

Over the past decade, novel characterisation techniques have been designed for monitoring void formation during composite manufacturing. Though a few studies mention the use of transparent tooling for the direct observation of near-surface porosity [10–12], most of them rely on XCT. This non-destructive characterisation technique allows 3D imaging of a specimen, obtained through the reconstruction of a series of planar X-ray projections equispaced along a 360° sample rotation. XCT can be used to monitor void formation in composite materials either via ‘in-situ’ or ‘ex-situ’ protocols. In ex-situ methods, composite specimens are produced outside of the scanner. The manufacturing process must be regularly interrupted to extract the sample and perform subsequent XCT characterisation [13,14]. Several authors relied on ex-situ methods to study void formation during the out-of-autoclave consolidation of epoxy-based carbon prepregs [15–17]. Laminates were prepared outside of the scanner, partially cured, cooled down to prevent further resin crosslinking, downsized, and finally subjected to XCT scanning. The disadvantage of an ex-situ approach is that information can only be extracted for the time step at which the experiment was interrupted and an XCT scan was taken [13,14]. The timing and the ordering of the changes that take place in between consecutive steps are lost. There is also an uncertainty related to the cooling rate in case the voiding process is very fast.

On the other hand, dynamic in-situ methods, i.e., an uninterrupted processing experiment with continuous data acquisition, allow real-time observation of microstructural changes [18–20] - including void formation in composites [13,14,21] - directly within the XCT scanner. Such scanning methods are often referred to as ‘dynamic 4D-XCT’, with time being the fourth dimension. Due to space restrictions, a miniature version of the process must be designed: the setup must fit and be able to rotate 360° inside the XCT system and should be made of thin, relatively low-atomic-number and low-density materials to minimise unwanted X-ray attenuation during scanning. More importantly, there is always a trade-off between scan speed and image quality, which makes the characterisation of small-scale dynamic phenomena, e.g., void growth, particularly difficult. Synchrotron X-ray sources may be used to circumvent this problem, but they are less accessible than lab-based XCT scanners. For these reasons, the first in-situ XCT experiments dedicated to void monitoring during composite manufacturing were developed only very recently. To our knowledge,

apart from Kratz [22] and Galvez-Hernandez [23], who made use of a lab-based XCT scanner, all other studies relied on synchrotron X-ray facilities [24–31]. Some authors studied the (de)consolidation of semi-finished products, i.e., prepreg or sheet moulding compounds, under heat and/or pressure [22,26,28,29,31]. Other research focused on liquid moulding (LM) techniques [25,27,30] but the in-situ analysis only covered the impregnation step and the setup consisted of a single fibre t, providing limited insights into the voiding mechanisms involved in real-scale LM processes.

Note that several laboratory-based 4D-XCT experiments dedicated to the monitoring of microstructural changes other than void formation in composites have been recently published. However, most of these studies make use of 'stepwise' instead of 'dynamic' 4D-XCT, which means that the experiment is interrupted to allow scanning the specimen at the highest possible spatial resolution. This may involve, for instance, applying a load increment to the specimen and scanning while the load is maintained at a constant value, before further increasing the load [32–34]. The few authors who made use of dynamic 4D-XCT *per se* [35–37] generally focused on phenomena occurring either at a larger length scale (on the order of a few hundred microns [35]) or at a slower rate (over the span of one or more hours [37]). This makes it easier, from a technical point of view, to find a satisfying trade-off between good-enough image resolution and reasonable scan time. To our knowledge, the work of Snels [36], dealing with the crystallisation of ice droplets, is the only lab-based 4D-XCT dynamic study combining a very small voxel size (~ 8 µm) with a short scan time (~ 15 s).

The objective of this study is twofold. First, a new lab-based XCT method is developed for the in-situ dynamic monitoring of void formation during vacuum infusion and curing of a thick (> 2 cm) glass fibre-reinforced polymer composite. The principle of the experimental setup used for in-situ infusion [38] is inspired by the work of Hemmer et al., who studied the evolution of the fibrous preform microstructure upon infusion of a non-reactive model fluid [39,40]. The mechanisms leading to void formation and transport are then investigated for the particular case of a 2.3 cm-thick methyl methacrylate (MMA)-based thermoplastic composite, produced by vacuum infusion of a dedicated monomer-based formula into a glass fabric layup and polymerisation within the preform. This system can potentially involve monomer boiling due to the exothermic and self-accelerating nature of the polymerisation reaction [41–44]. It can also be prone to void formation through common mechanisms including flow-related void entrapment during the impregnation step.

2 Experimental methods

2.1 Materials

Composite preforms were made of quasi-unidirectional HiMax^{TM} XGE190 bi-axial non-crimp glass fabric (Hexcel, XCT, USA) with an areal weight of 3.791 kg.m^{-2}. The thermoplastic resin, which has been formulated to ensure compatibility with liquid composite moulding technologies, comprised an infusion-grade MMA-based monomer formula (Elium® 151 OSA of Arkema, France) and a ketone peroxide thermal initiator (Butanox® M-50 of Nouryon, The Netherlands). The consumables for bagging were obtained from Diatex SAS (France).

2.2 Miniature infusion setup

The downsized infusion setup was designed based on the work of Hemmer et al. [39,40], who studied with XCT the microstructural evolution of a glass fabric preform upon in-situ infusion with a non-reactive fluid. The original setup of Hemmer consisted of a PVC plate pierced with holes for connecting the resin and vacuum lines, and was used for the infusion of a 9 mm-thick glass fabric stack. The setup manufactured in this work [38] is shown in Fig. 1, alongside the associated coordinate system. The following upgrades and elements of novelty were introduced: (1) the addition of a heating system, (2) the addition of a dedicated rotating mount shown in Fig. 1c and (3) the use of thermally conductive materials. Note that the materials used for manufacturing and operating the setup are detailed in Table A1 of Appendix A. Aluminium was used as the main constituent of the setup for its combination of high thermal conductivity and relatively low density, compared to other metals.

Images may appear blurred during proofing as they have been optimized for fast web viewing. A high quality version will be used in the final publication. Click on the image to view the original version.

alt-text: Fig 1:

Fig. 1

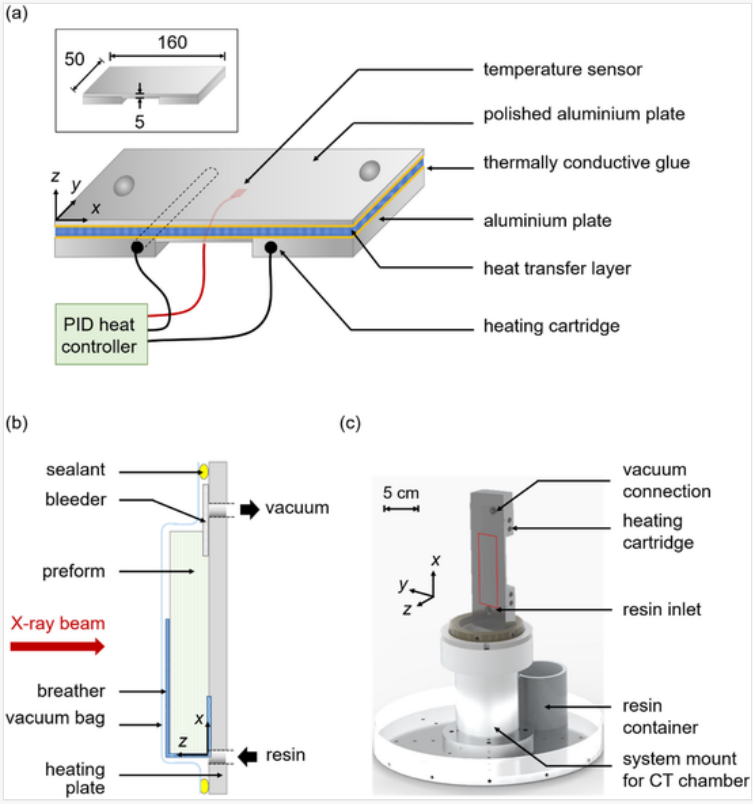

Design of the miniature infusion setup: (a) structure and dimensions in mm, (b) simplified side view of the setup and preform during XCT scanning and (c) 3D view of the setup installed in the XCT chamber. The red rectangle indicates the preform location.

2.3 In-situ infusion experiment

2.3.1 Preparation

Composite specimens were manufactured using the miniature infusion setup illustrated in Fig. 1. Preforms were produced by laying up 10 glass fabric plies of dimensions L = 9 cm and w = 4 cm onto the heating plate. The final preform thickness h was close to 2.3 cm. The tow orientation is parallel to the x-axis (i.e., the infusion direction).

The layup was wrapped with a peel ply to prevent any stray glass filaments from compromising the bagging step. As described in Fig. 1b, strips of breather and bleeder materials were positioned onto and underneath the preform to improve resin flow and vacuum distribution, respectively. The vacuum bag was installed onto the edges of the heating plate using 6 mm-wide strips of mastic sealant, and pleated according to standard bagging practices. The tubing for the resin inlet and vacuum line was connected to the back of the setup using pneumatic elbows. The setup was screwed onto a dedicated rotating mount in the XCT chamber, see Fig. 1c. Connections to an external vacuum pump and heating controller were achieved via slip ring connectors (to enable setup rotation during scanning) and vacuum-tight gate valves. Loose tubes or cables were secured out of the field of view of the detector using adhesive tape. Pictures of the installed setup are presented in Fig. 2. The composite preform was subjected to 200 mbar vacuum conditions and left to degas and stabilise for one hour, as described by Hemmer [39,40].

Images may appear blurred during proofing as they have been optimized for fast web viewing. A high quality version will be used in the final publication. Click on the image to view the original version.

alt-text: Fig 2:[Instruction: Is it possible to make the figure slightly bigger (in the single column format) ?]

Fig. 2

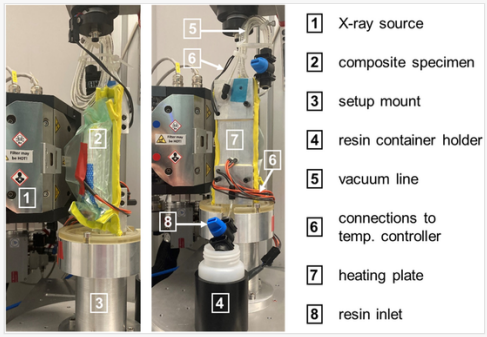

Front (left picture) and back (right picture) views of the infusion setup after installation in the XCT chamber.

2.3.2 In-situ infusion experiment

The resin mix was prepared with 1.5 parts initiator per hundred parts monomer formula, mechanically stirred for 5 min, and then degassed for 1 min at 100 mbar. The time at which the initiator was added is referred to as t_0. Between t_0 and t_0 + 8 min, the resin container was secured inside the XCT chamber using the dedicated holder shown in Figs. 1c and 2 . Resin infusion was then carried out under 200 mbar vacuum and at room temperature. Complete filling of the preform was achieved within 2 minutes of infusion (i.e., around t_0 + 10 min), after which the valves connecting the setup to the resin inlet and vacuum line were closed. In-situ dynamic scanning started around t_0 + 12 min, and the temperature controller was switched on. The infused preform was heated from the initial chamber temperature (i.e., 30°C) to 80°C, with a heating rate close to[Instruction: No line break between "heating rate close to" and "7°C.min-1"]

7°C.min^{-1}. The setup temperature was maintained at 80°C until a sharp temperature peak was reached at the surface of the preform, indicating the completion of the polymerisation reaction [43,45]. The setup was then left to cool down to a stable temperature, which was close to 40°C. After the dynamic scanning was finished, a final static scan of the composite specimen was taken.

Note that, prior to performing the in-situ 4D-XCT experiment, a preliminary infusion test was performed outside the scanner in the same conditions as those described in the previous paragraph [38]. Among other things, this ‘ex-situ’ test allowed verifying that the setup rotation and X-ray irradiation during scanning did not have a significant influence on void morphology and distribution in the composite specimen. The outcomes of this ex-situ experiment are presented in Appendix B.

2.4 XCT scanning parameters

3D imaging of the composite specimens was performed at the KU Leuven XCT Core Facility on a 230 kV/300 W TESCAN UniTOM XL system, with the setup mount rotating 360° around the *x*-axis of the composite sample. A tungsten target was installed on the reflection source together with a 0.1 mm thick CuZn filter to harden the X-ray beam. Two different acquisition modes, referred to as ‘dynamic’ and ‘static’, were applied during the experiment. Both acquisition methods applied a tube voltage of 150 kV and a tube power of 15 W. The dimensions of the field of view (FOV) were set to 25, 30 and 20 mm in the *x, y* and *z*-directions, respectively, meaning that neither the uppermost glass fabric ply, nor the lateral edges of the preform (along the *y*-axis) were observed. A compromise had to be found between enlarging the field of view and better spatial resolution, achieved in this case by reducing the source-to-setup distance. Enlarging the source-to-detector distance to increase the spatial resolution was avoided, as this would have been detrimental to the temporal resolution of the dynamic acquisition.

Dynamic scanning was initiated after infusion and covered the whole duration of the polymerisation and cooling steps. Static scanning was used to image the specimen in its final state, i.e., after the complete cooling of the setup. The purpose of the static scan was to operate the best possible spatial resolution with the in-situ setup installed. The associated scan time did not matter in this case, as no time-dependent phenomena were expected to occur. A voxel edge size of 11.25 µm was obtained in static acquisition mode. 2400 radiographic projections were acquired with projection averaging set to 2 to improve the signal-to-noise ratio, at an exposure time of 275 ms, resulting in a scan time of 23 minutes. On the other hand, in dynamic acquisition mode, the scan time had to be short enough to capture subtle changes in void pattern over time. The scan speed was gained by sacrificing image quality through larger rotation steps, detector binning, and disabling projection averaging. In this specific case, a 2 × 2 binning of the detector was applied

(i.e., each 2×2 matrix of pixels was combined into one larger pixel). This doubles the voxel edge size (i.e. 22.5 μm) compared to the static experiment but, at the same time, provides a better signal-to-noise ratio and shorter exposure time (150 ms), which leads to a reduced number of radiographic projections (900). 60 continuous 360° acquisitions at a temporal resolution of 135 seconds resulted in a duration of 135 minutes for the dynamic experiment.

After the static scan, the composite specimen was subjected to further 'post-mortem' characterisation as follows: the laminate (of dimensions L = 9 cm, w = 4 cm and $h \sim 2.3$ cm, see section 2.3.1) was released from the setup and downsized using a water-cooled disc milling cutter. A cuboid sample of approximate dimensions $12 \times 10 \times h$ mm^3 was extracted from the central part of the specimen (i.e., close to coordinates $x = L/2$ and $y = w/2$), and subjected to XCT scanning with a voxel size of 5 μm. The number of radiographic projections was set to 3000 and the scan time was close to 55 min; the other XCT acquisition parameters remained constant with respect to the static scan. The cuboid sample shape was selected to allow decreasing the voxel size compared to the static scan, while keeping a FOV sufficiently large for providing representative results in terms of void pattern.

2.5 Processing of XCT results

The software Panthera (V. 1.3b1, TESCAN XRE NV) was used to reconstruct the XCT scans and export cross-sectional images. The open-source software ImageJ [46] was used to further analyse some of the 2D cross-sectional images, while post-processing of the 3D data was performed in Avizo 2021.2 (ThermoFisher). Prior to the quantitative analysis, noise filtering was applied, using a median filter with the neighbourhood connectivity set to 26 and 3 iterations. The median filter reduces the photon noise in the scanned volume. Next, greyscale thresholding was performed to segment the images into three phases, i.e., voids, matrix and glass fibre tows. To maintain consistent sensitivity in the detection of voids, the same set of segmentation parameters was applied to all 60 time steps of the dynamic scan.

3 Results and Discussion

3.1 Cross-sectional images of the composite specimen upon processing

2D cross-sectional images were extracted from each of the 60 reconstructed time steps of the dynamic scan at a fixed location, i.e., in the (xoz) plane intercepting the y-axis at $y = w/2$. The corresponding images are displayed in Figs. 3 and 4. Each phase of the material (i.e., fibres, resin and voids) is characterised by a different shade of grey: glass fibre tows appear light grey, while the resin looks darker and the voids are black. The red rectangles in Figs. 3 and 4 serve as a guide and indicate regions where a significant change in void morphology is observed as compared to the time step before. Note that only one image is presented for time steps 1 and 2 in Fig. 3, and for time steps 8 to 60 in Fig. 4, as no significant change in void pattern was found within these two series of images.

Images may appear blurred during proofing as they have been optimized for fast web viewing. A high quality version will be used in the final publication. Click on the image to view the original version.

alt-text: Fig 3:

Fig. 3

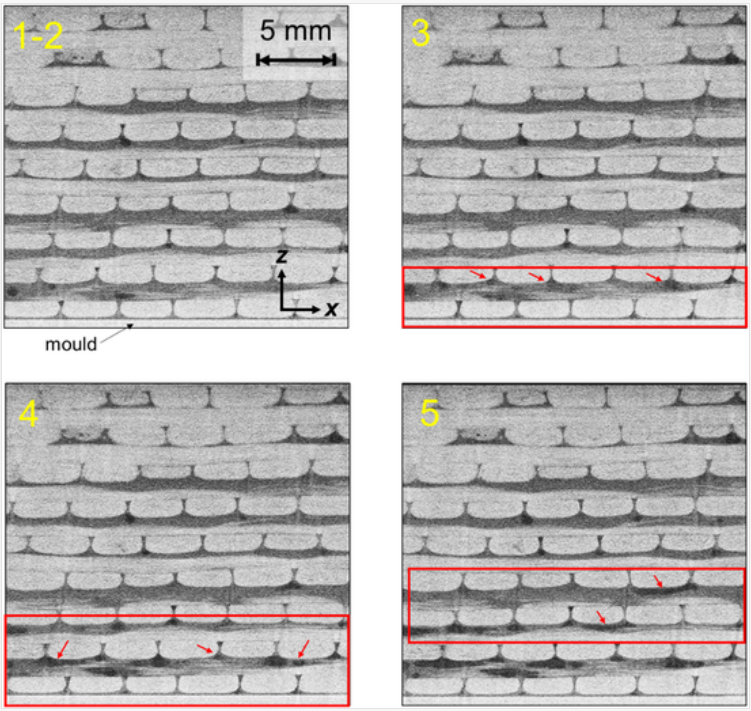

Reconstructed xz slices extracted from the dynamic acquisition in time steps 1 to 5 at $y = w/2$. Red boxes indicate areas where void patterns noticeably change compared to the same area of the previous time step. Within the boxes, arrows highlight a few examples of voids presenting a significant evolution in shape or size with respect to the previous time step.

Images may appear blurred during proofing as they have been optimized for fast web viewing. A high quality version will be used in the final publication. Click on the image to view the original version.

alt-text: Fig 4:

Fig. 4

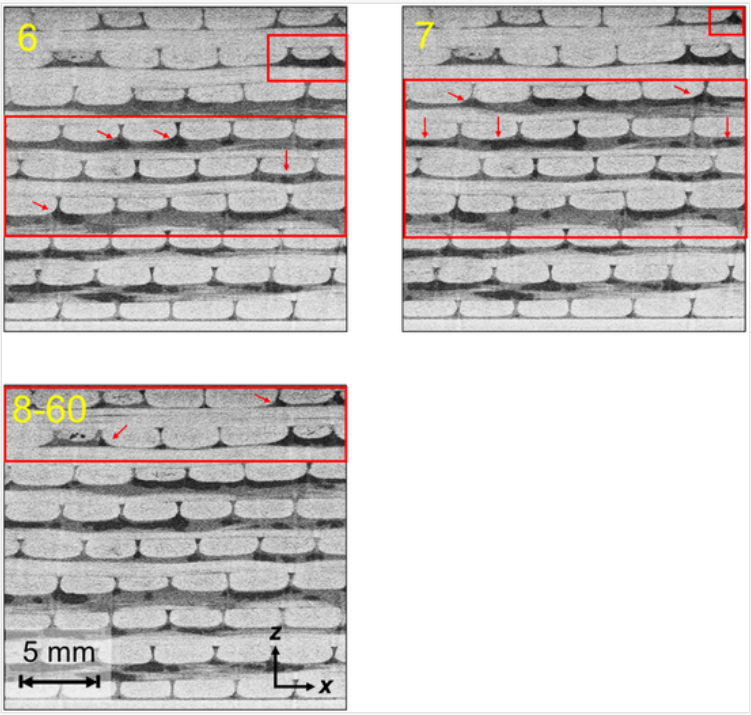

Reconstructed xz slices extracted from the dynamic acquisition in time steps 6 to 60 at $y = w/2$. Red boxes indicate areas where void patterns noticeably change compared to the same area of the previous time step. Within the boxes, arrows highlight a few examples of voids presenting a significant evolution in shape or size with respect to the previous time step.

The cross-sectional images presented in Figs. 3 and 4 reveal that the vast majority of void formation events occur between time steps 2 and 8, i.e., within the first 30 minutes following peroxide introduction, though a few randomly distributed voids are already present in time steps 1–2. Second, voids are exclusively detected in between two subsequent fabric plies and/or in between fibre tows of the same ply. The smallest dimension of the voids is on the order of a few hundred microns. Third, void growth takes place gradually along the z-axis between time steps 2 and 8, i.e., voids nucleate first in the lower plies, i.e. in the region near the mould (see time steps 3 and 4 of Fig. 3). Once these voids have attained their final size, other voids start growing in the plies located above (see time steps 5 to 8). This continues until the surface of the preform is reached (time step 8), after which the void pattern does not evolve anymore.

3.2 Evolution of porosity

The average volume fraction of voids in the composite, which will be referred to as the porosity Φ, was estimated for each of the 60 time steps in the dynamic scan. The heating plate was cropped out of the FOV as it would interfere with the determination of the porosity. Then, the value of Φ was calculated for each time step. The evolution of Φ is presented in Fig. 5 as a function of the time step in the dynamic experiment and its corresponding experimental time (for which the origin is defined as t_0, i.e., peroxide introduction). The evolution of the specimen's surface temperature $T_{surface}$ is also included, alongside with two examples of 3D void pattern renderings obtained from time steps 1 and 8. As no significant evolution in porosity was found beyond time step 10, only one Φ value is represented for steps 11 to 60. It was obtained from time step 51, which was acquired after the preform had cooled down to a stable temperature and is thus considered representative of the final state of the system.

Images may appear blurred during proofing as they have been optimized for fast web viewing. A high quality version will be used in the final publication. Click on the image to view the original version.

alt-text: Fig 5:[Instruction: This figure should be larger, e.g. spread over two columns]

Fig. 5

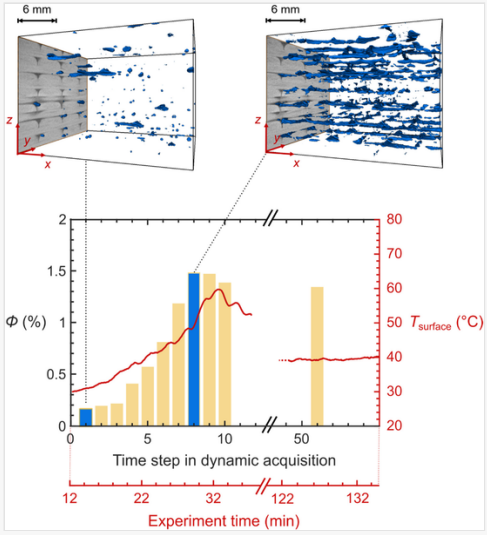

Variation of the average porosity Φ over the volume of interest and evolution of the surface temperature $T_{surface}$ as a function of the experiment time and corresponding time step in the dynamic acquisition. 3D volume renderings of the void patterns generated from time steps 1 (top left) and 8 (top right) during the dynamic acquisition are also presented.

The information displayed in Fig. 5 consolidates the assumptions made from the cross-sectional images. In particular, Φ for time step 1 is not equal to zero but close to 0.2 %, which confirms the presence of voids in the composite before the start of the dynamic acquisition. The 3D rendering of time step 1 reveals a homogenous, random-looking distribution of these voids throughout the scanned volume, which was also inferred from the 2D images. Secondly, Fig. 5 allows

verifying that void formation/growth events exclusively occurred between time steps 1 and 8, as shown by the continuous increase of Φ from ≈ 0.2 % at time step 1 up to the maximum value of[Instruction: no line break between "maximum value of" and "phi = 1.5%"]

Φ ≈ 1.5 % at time step 8. The slight drop in the calculated Φ between time steps 8 (Φ = 1.49 %) and 51 (Φ = 1.35 %) will be discussed in the next section, as more information is required to confirm the existence of a relationship between this small, apparent decrease in porosity and an actual change in void pattern between time steps 8 and 51.

The results shown in Fig. 5 provide a way to relate the evolution of Φ with the timeline of the polymerisation reaction, through the temperature plot. As mentioned in the introduction, MMA polymerisation exhibits a characteristic thermokinetic behaviour. In the early stages of monomer conversion, the temperature of the reaction medium increases slowly and steadily. Then, self-acceleration occurs: the temperature increases more and more rapidly until reaching a peak, which corresponds to the completion of the reaction. Finally, the polymerisation medium cools down back to room temperature. The surface temperature of the preform reaches its maximum value (i.e., 60°C) around 30 min after the peroxide introduction, which corresponds to the end of time step 9. Therefore, the first 9 time steps cover the polymerisation step, while the rest of the experiment covers the cooling step. The rates at which $T_{surface}$ and Φ values increase during polymerisation follow a similar evolution, i.e., both parameters increase faster as time passes by, until the maximum temperature is reached. This further highlights the direct link existing between the polymerisation reaction, temperature and void formation/evolution in the composite specimen.

3.3 Evolution of void size

The size of the voids can be characterised for each of the dynamic time steps via a 3D local thickness (LT) analysis. This operation consists in automatically fitting spheres inside each void, starting from the largest possible diameter values. For each time step, a distribution of the cumulated volume of the inscribed spheres as a function of their diameter can be plotted, which is one way of determining the void 'size'. Compared to other procedures aiming at characterising void shapes and dimensions, e.g., in terms of their Feret diameter, the LT analysis has the advantage of limiting the influence of noise (which can give rise, e.g., to spurious connectivity between adjacent voids) on the results.

The results of the LT analysis of the voids captured by time steps 1, 5, 8 and 51 are displayed in Fig. 6. The amplitude of the distributions evolves similarly to the porosity Φ, i.e. it increases between time steps 1 and 8 and then slightly decreases between time steps 8 and 51. The range of LT values remains relatively unchanged, extending from 50 to ≈ 800 µm in all cases. As Φ increases, two distinct populations appear within the void size distributions, as depicted by the orange and red boxes in Fig. 6. The orange and red boxes contain LT values below and above ≈ 500 µm, respectively. The former can be attributed to inter-ply voids, while the latter is characteristic of inter-tow voids forming within the V-shaped spaces between two adjacent fibre tows belonging to the same ply. As illustrated in Fig. 6, these two categories can interconnect into a single, large void. The architecture of the fibrous preform constrains the expansion of the voids in the *z*-direction, resulting in more and more elongated cavities in the *x* and *y*-directions as Φ increases. As shown by the 3D volume rendering of time step 8 in Fig. 5, this results in a partial or full coalescence of the voids in planes perpendicular to the *z*-direction.

Images may appear blurred during proofing as they have been optimized for fast web viewing. A high quality version will be used in the final publication. Click on the image to view the original version.

alt-text: Fig 6:

Fig. 6

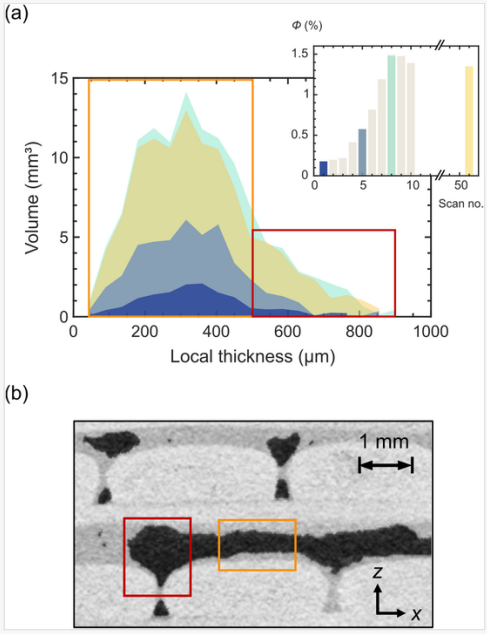

Void types and void size distribution: (a) local thickness analysis of the voids determined from time steps 1, 5, 8 and 51. The orange and red boxes correspond to inter-ply voids and inter-tow void populations, respectively. (b) 2D *xz* cross-sectional image showing examples of the two categories of voids, using boxes of the same colour.

Last, comparing the size distributions of the voids at time steps 8 and 51 reveals a slight and homogenous decrease in the volume of the voids, regardless of size. More precisely, the *total* volume of the voids in the region of interest drops by 8.1 % between steps 8 and 51, i.e., during cooling of the composite preform. This is the same order of magnitude as the measured drop of 9.6 % in Φ that was mentioned earlier. The slight discrepancy between the LT analysis and calculated porosity values can be easily explained by superimposing *xz* cross-sectional images of time steps 8 and 51 (taken at the $y = w/2$ location) and projecting the measured standard deviation in greyscale for each pixel via the 'Z project' tool of ImageJ. The standard deviation map is presented in Fig. 7. The white areas indicate the locations where significant differences have been detected between the two images. There is a clear vertical shift (i.e., along the *z*-axis) between the two images, which becomes larger as the *z* coordinate increases. This vertical contraction of the material results from the thermal shrinkage experienced by the composite during cooling. Note that the heterogenous contraction in the *z*-direction is likely present because the surface plies, which are closer to the bag, cool down faster through air convection than the bottom plies, which are in contact with a thick layer of metal (that was previously heated).

Images may appear blurred during proofing as they have been optimized for fast web viewing. A high quality version will be used in the final publication. Click on the image to view the original version.

alt-text: Fig 7:

Fig. 7

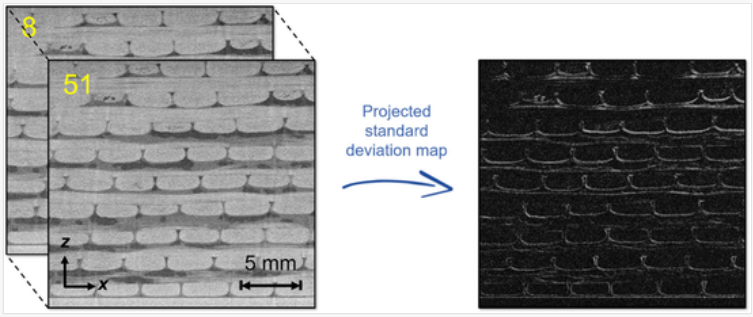

xz cross-sectional images of time steps 8 and 51 (left), and their projected pixel-by-pixel standard deviation map (right), obtained via the Z project tool in ImageJ.

Thermal shrinkage thus affects the relative proportions of voids, matrix and fibre tows within the fixed field of view used for the determination of the porosity. This explains the discrepancy between the calculated drop in porosity due to thermal shrinkage and the estimated drop based on the LT analysis of the voids.

3.4 Assessment of dynamic scan uncertainty

The static scan and one of the last time intervals in the dynamic acquisition, i.e., time step 51, were compared to verify the representativeness of the dynamic scanning method in terms of void size. As mentioned previously, the two datasets were both acquired after the system had completely cooled down and was no longer expected to evolve. The distributions of LT values obtained via both scanning methods are presented in Fig. 8. The plots are relatively similar, which confirms the ability of the dynamic scanning method to capture the void dimensions with reasonable accuracy. This also gives confidence in the fact that the resolution of the dynamic acquisition mode is sufficient to capture the entire void size distribution, including at least most of the smaller voids; otherwise, there would have been a shift to the left for the curve in the static acquisition.

Images may appear blurred during proofing as they have been optimized for fast web viewing. A high quality version will be used in the final publication. Click on the image to view the original version.

alt-text: Fig 8:

Fig. 8

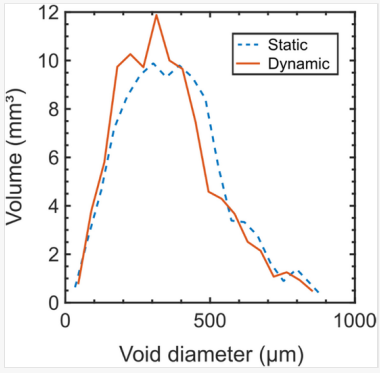

Local thickness analysis of the voids after cooling, determined from dynamic scanning (time step 51) versus static scanning.

Note that the LT values of the voids captured by the dynamic scan are systematically higher than those obtained from the static scan in the 150–400 μm range, while the opposite trend is observed in the 400–550 μm range. This results in a significantly higher Φ value for the static scan (≈ 1.9 %) compared to the dynamic scan (≈ 1.3 %). In this case, the mismatch is probably due to a more precise detection of the edges of the voids in the higher-resolution static scan. However, both porosity values are in the same range, which is deemed sufficient with respect to the purpose of this study focused on the identification of the void formation mechanisms.

Nonetheless, it is important to recall that the voxel size of the static scan is close to 11 μm, and that - according to the rule of thumb -, XCT scanning can only decently render features that are at least three times larger than the voxel size due to image resolution limits and the partial volume effect. This implies that for voids having their smallest dimension below 30–35 μm this can significantly reduce the accuracy of the quantification. Fig. 9 displays the 3D rendering of the voids obtained from the 'post-mortem', high-resolution XCT scanning of the downsized composite specimen mentioned at the end of section 2.4. The voids depicted in brown are those captured with high fidelity via dynamic scanning, as their smallest dimension exceeds 66 μm (i.e., 3 times the voxel size of the dynamic scan). The other voids, which are shown in green, have their smallest dimension below this threshold value. These 'micro-voids' do not exceed a few voxels in size and their smallest dimension is generally equal to a single voxel (i.e., 5 μm), which explains why they were not captured either by the dynamic scan nor by the static scan performed at the end of the in-situ experiment. They appear either spherical or slightly ellipsoidal, and are almost exclusively found *within* the fibre bundles, in the narrow matrix pockets separating glass filaments. However, and perhaps more importantly, this population of micro-voids only accounts for about 11 % of the total porosity of the downsized composite specimen. This further confirms that the dynamic scanning method is able to capture the majority of the porosity developing in the composite system of interest.

Images may appear blurred during proofing as they have been optimized for fast web viewing. A high quality version will be used in the final publication. Click on the image to view the original version.

alt-text: Fig 9:

Fig. 9

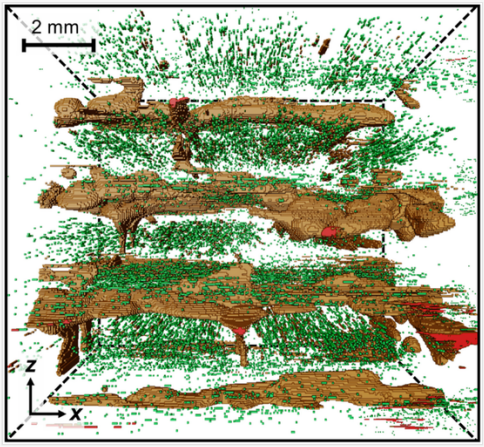

3D volume rendering of the voids obtained from the post-mortem characterisation of the composite specimen by high-resolution XCT. Voids whose smallest dimension exceeds 66 μm appear in brown, while the others appear in green.

4 Discussion on void formation mechanisms

In light of the results presented in Figs. 3 to 6 and the main sources of porosity identified from the literature, the following timeline and explanations are proposed with respect to the void formation events occurring in the Elium® composite. First, a small amount (≈ 15 %) of the final volume of the voids arises from the infusion step, during which voids may form through the degassing of the resin and/or through the flow-related entrapment of voids during preform filling. In this work, the resin was degassed prior to infusion at a pressure lower than the infusion pressure. Therefore, it is assumed that the few voids observed within the preform after infusion result from flow-induced entrapment upon preform filling. Additionally, the post-mortem high-resolution XCT characterisation of the specimen reveals the presence of numerous micron-sized voids within the fibre bundles (cf. Fig. 9), which are too small to be captured by the dynamic scan. These are characteristic of a higher resin flow rate in between the bundles (viscous flow) during preform filling, compared to the capillary flow taking place at a slower pace within the bundles, see e.g. [5,47].

The majority of void growth events in the Elium® composite are attributed to the in-situ polymerisation step, during which they appear gradually along the thickness direction of the preform, starting from the lower plies close to the heating plate. According to the literature, the two possible causes for cavitation during polymerisation are the boiling of one or several resin component(s) (or by-product(s)) and/or the chemical shrinkage of the resin. The boiling of the Elium® monomer MMA within thick composite parts produced by vacuum infusion has been thoroughly studied in references [43,45]. Assuming the pressure inside the bag raises back to around 1 atm after infusion (which should be the case after closing the resin inlet and vacuum lines [48,49]), the boiling temperature of MMA should be close to 101°C within the bag. The Elium® composite specimen reached a maximum surface temperature of 60°C during polymerisation (as recorded by the thermocouple), and a maximum mould temperature of 80°C (as measured by the PID heating system). Therefore, it seems unlikely that the MMA boiled within the preform. Furthermore, the spatial distribution of inter-ply voids after polymerisation displays no significant trend along the *z*-axis of the preform, see Fig. 10. In the case where void formation results from monomer boiling, a characteristic gradient pattern is observed across the thickness of the preform: the higher the *z*-coordinate, the higher the inter-ply porosity [43,45,50].

Images may appear blurred during proofing as they have been optimized for fast web viewing. A high quality version will be used in the final publication. Click on the image to view the original version.

alt-text: Fig 10:

Fig. 10

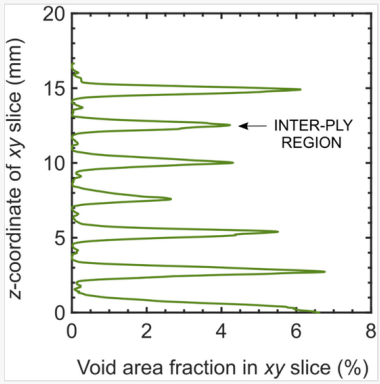

Distribution of the voids along the z-axis of the FOV at time step 51
(i.e. after polymerisation and cooling).

Progressive preform decompaction, resulting from the closing of the vacuum line after the infusion step, is another possible cause for the extensive void growth observed over the first 9 time steps of the experiment. This phenomenon is not, in general, listed among the possible sources of void formation likely to affect composites processed by liquid moulding. It is common practice to keep the vacuum line open to ensure a continuous removal of air and excess resin, thus maintaining proper vacuum pressure throughout the infusion process, until the polymer resin has fully infused and cured. However, due to the high volatility of the Elium® monomer, it is preferable to close both the resin and vacuum lines just after infusion [43]. Using the measuring tool of ImageJ [46] along the *z*-axis of each *xz* slice, the distance *d* between the mould and the bottom of the 9th ply was obtained for each time step of the dynamic scan. For a given time step *i*, the thickness increase Δd_i is expressed as *d*(time step *i*) – *d*(time step 1). The evolution of Δd over the course of the in-situ experiment is shown in Fig. 11, alongside the surface temperature and mould temperature plots. There is, indeed, a significant increase in preform thickness in the early stages of polymerisation, i.e., between time steps 1 and 4. From time steps 5 to 9, the value of Δd reaches a plateau around 220 μm, before dropping back to 0 between time step 10 and the end of the dynamic scan. As a matter of fact, the evolution of Δd is clearly correlated with those of the mould and preform temperatures, which are plotted in red in Figure 11. We can therefore conclude that the preform only experiences temporary decompaction, which is merely related to the thermal dilation of the composite material upon heating. If the laminate was subjected to deconsolidation due to a pressure increase in the system, the variation in laminate thickness would be irreversible, which is not the case here.

Images may appear blurred during proofing as they have been optimized for fast web viewing. A high quality version will be used in the final publication. Click on the image to view the original version.

alt-text: Fig 11:[Instruction: this figure should be larger, though it can remain in a single column format]

Fig. 11

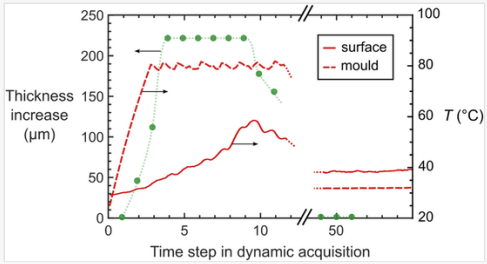

Thickness increase of the laminate over the dynamic scanning sequence; the dotted green line only serves as a guide for the eye. The temperature plots measured at the surface of the preform and within the heating mould are displayed in red.

By elimination, chemical shrinkage therefore appears as the most probable source of void formation in the Elium® composite of interest. This hypothesis is further supported by the fact that poly(methyl methacrylate) (PMMA), which is the main constituent of Elium® after polymerisation, is known to be around 20 % denser than the MMA monomer [51].

Finally, there is a very slight reduction in void size upon cooling of the composite specimen as a consequence of thermal shrinkage. This translates into a small but significant decrease in the calculated value of Φ after the end of the polymerisation reaction.

5 Conclusions and perspectives

This study provides a proof of concept for a novel 4D-XCT lab-based experiment aimed at monitoring the processing of composites by vacuum infusion and in-situ polymerisation. The key focus was placed on void formation. The main outcomes of the study are the following: (1) the design, manufacturing and successful testing of a miniature heating infusion setup, (2) the characterisation by XCT of void formation and growth events in a composite preform during matrix polymerisation and (3) a quantitative assessment of the nucleation, growth and coalescence process in terms of shape, size, and location of the voids. Using this new method, chemical shrinkage has been identified as the principal source of porosity in the composite system of interest, i.e., a thick glass fibre-reinforced Elium® laminate.

Laboratory-based XCT systems have technical limitations which make it difficult to perform dynamic experiments with both a high spatial resolution and temporal resolution. In this work, the best possible trade-off we could find led to a scan time of 2 min 15 and a voxel edge size of 22 µm. The scan time is too long to fully capture the void nucleation and growth events in a viscous liquid [52], while the voxel size is too large for distinguishing individual fibres within the tows and detecting voids smaller than a few tenths of microns. While using a synchrotron X-ray light source would certainly help to overcome these limitations, this would bring in turn several new challenges [7] - although ongoing advancements in computing may render this statement obsolete within a few years. First, the field of view would be reduced, decreasing the probability of capturing several void formation events. Second, the high luminosity of synchrotron sources would certainly cause self-heating of the setup, which - in the case of Elium® - could cause monomer boiling and subsequent void formation. Finally, the large amount of data generated by synchrotron XCT scanning would make it more difficult to monitor the entire polymerisation of Elium® with continuous acquisition.

CRediT authorship contribution statement

Sarah F. Gayot: Writing – original draft, Visualization, Validation, Project administration, Methodology, Investigation, Conceptualization. **Jeroen Soete:** Writing – review & editing, Validation, Resources, Methodology, Investigation, Formal analysis, Data curation, Conceptualization. **Johan Vanhulst:** Resources, Methodology, Conceptualization. **Pierre Gérard:** Supervision, Resources. **Thomas Pardoen:** Writing – review & editing, Supervision, Resources, Funding acquisition.

Declaration of competing interest

The authors declare that they have no known competing financial interests or personal relationships that could have appeared to influence the work reported in this paper.

Acknowledgements

Financial support from Arkema and from the KU Leuven project no. C24/17/052, (regarding in-situ X-ray XCT characterisation of composite materials and tissues during mechanical testing) is gratefully acknowledged. The FWO large infrastructure I013518N project is also acknowledged for their financial support of the X-ray infrastructure, as well as the KU Leuven XCT Core Facility for the 3D & 4D image acquisition and quantitative post-processing tools (https://xct.kuleuven.be/). The authors would also like to thank the Elium team at Groupement de Recherche de Lacq (Lacq, France) for helping design the bagging protocol for the miniature setup. Finally, the authors wish to address their warm thanks to Dr. Florent Hannard, for his guidance and assistance with image processing, and Prof. Yentl Swolfs, for the insights he provided with respect to synchrotron scanning. The authors extend their sincere appreciation to Prof. Christian Bailly for his help in understanding the aspects related to polymer physics and polymerisation thermokinetics.

Appendix A

alt-text: Table A1

Table A1

The table layout displayed in this section is not how it will appear in the final version. The representation below is solely purposed for providing corrections to the table. To view the actual presentation of the table, please click on the Preview located at the top of the page.

Material used for assembling and operating the infusion setup.

Description of the part	Reference or characteristics	Manufacturer
Polished aluminium plate	160 × 50 × 1 mm^3	-
Heat transfer layer	MHP-2550A100A	AMEC Thermasol
Ceramic cartridge heaters	12 V 40 W, ∅ 6 × 20 mm3	Reprap
Temperature sensors	LM35CAH	Texas Instruments
Wire connectors	Micro Mate-N-Lock	TE Connectivity
Thermally conductive glue	TC-2810	3M
Elbow pneumatic connectors	3199 04 19, 4 mm	Legris
Heating controller	Love 32B-22-LV	Dwyer Controls
Power supply	24 V/5A	-
Slip ring	SRH 1254	Gileon
Vacuum pump	XL 20	PIAB
Resin/vacuum PUER tubing	1025U04R08, 4 mm	Legris
Manual pneumatic valve	7910 04 00	Legris
Remote pneumatic valve	VX220AGA	SMC
Vacuum gauge	GZ46-K-02	SMC

Appendix B

The composite specimen manufactured ex situ as part of a preliminary test of the infusion setup has been processed, downsized and subjected high-resolution XCT scanning as follows. The manufacturing conditions were similar to those applied during the in-situ experiment, apart from the vacuum pump which was different. More precisely, the pump used for the ex-situ test was more powerful than that used for the in-situ experiment, resulting in a lower pressure within the preform (50 mbar vs. 200 mbar for the in-situ test). After polymerisation and cooling, the ex-situ specimen was demoulded, downsized and subjected to high-resolution XCT scanning as described at the end of section 2.4.

The 3D rendering of the voids is presented in Fig. B1, using the same colour code as for Fig. 9. The composite specimen manufactured ex situ (i.e., without sample rotation nor X-ray irradiation) displays the same two void populations as those previously identified for the in-situ specimen: the small, relatively spherical intra-tow voids, and the larger, very elongated type of voids (which are observable via dynamic scanning). The relative proportions of both populations are in the same order of magnitude as for the in-situ sample, with the larger voids (> 66 μm) accounting for 81.5 % of the total porosity in terms of volume fraction. The location and morphology of both types of voids are consistent with respect to the results obtained from the in-situ sample, i.e., the larger voids form in the interply area and have their smallest dimension in the order of a few hundred microns, and the smaller ones form within the fibre bundles, and are only a few microns in size. We can therefore conclude that sample rotation and exposition to X-rays during the in-situ experiment does not disturb the void formation process significantly.

Images may appear blurred during proofing as they have been optimized for fast web viewing. A high quality version will be used in the final publication. Click on the image to view the original version.

alt-text: Fig B1

Fig. B1

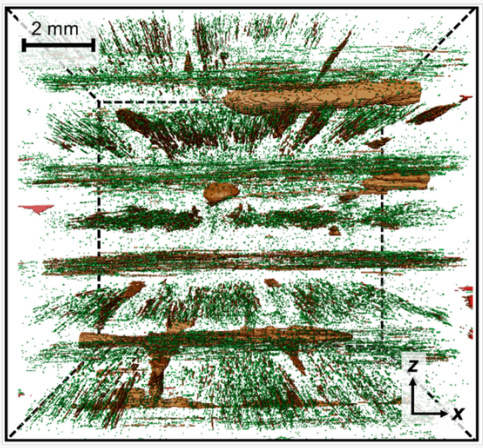

3D volume rendering of the voids obtained from the post-mortem characterisation of the composite specimen manufactured ex situ by high-resolution XCT. Voids whose smallest dimension exceeds 66 μm are depicted in brown, while the others are shown in green.

References

The corrections made in this section will be reviewed and approved by a journal production editor. The newly added/removed references and its citations will be reordered and rearranged by the production team.

[1] Kardos JL, Dave R, Dudukovic NP. Voids in composites. the manufacturing science of composites, Proceedings of Manufacturing International ’88, vol. 4, Atlanta, Georgia (USA): ed. TG Gutowski; 1988, p. 41–8.

[2] TS Lundstrom, BR Gebart, CY. Lundemo, Void Formation in RTM, J. Reinf. Plast. Comp. 12 (1993) 1339–1349, doi:10.1177/073168449301201207.

[3] N Patel, V Rohatgi, LJ. Lee, Micro scale flow behavior and void formation mechanism during impregnation through a unidirectional stitched fiberglass mat, Polym. Eng. Sci. 35 (1995) 837–851, doi:10.1002/pen.760351006.

[4] M Afendi, W Banks, D. Kirkwood, Bubble free resin for infusion process, Compos. Part A Appl. Sci. Manuf. 36 (2005) 739–746, doi:10.1016/j.compositesa.2004.10.030.

[5] M Mehdikhani, L Gorbatikh, I Verpoest, SV. Lomov, Voids in fiber-reinforced polymer composites: A review on their formation, characteristics, and effects on mechanical performance, J. Compos. Mater. 53 (2019) 1579–1669, doi:10.1177/0021998318772152.

[6] Birt EA, Smith RA. A review of NDE methods for porosity measurement in fibre-reinforced polymer composites. Insight - Non-Destructive Testing and Condition Monitoring 2004;46:681–6. https://doi.org/10.1784/insi.46.11.681.52280.

[7] E Maire, PJ. Withers, Quantitative X-ray tomography, Int. Mater. Rev. 59 (2014) 1–43, doi:10.1179/1743280413Y.0000000023.

[8] G Mayr, B Plank, J Sekelja, G. Hendorfer, Active thermography as a quantitative method for non-destructive evaluation of porous carbon fiber reinforced polymers, NDT E Internat. 44 (2011) 537–543, doi:10.1016/j.ndteint.2011.05.012.

[9] H Jeong, DK. Hsu, Experimental analysis of porosity-induced ultrasonic attenuation and velocity change in carbon composites, Ultrasonics. 33 (1995) 195–203, doi:10.1016/0041-624X(95)00023-V.

[10] R Helmus, J Kratz, K Potter, P Hubert, R. Hinterhölzl, An experimental technique to characterize interply void formation in unidirectional prepregs, J. Compos. Mater. 51 (2017) 579–591, doi:10.1177/0021998316650273.

[11] W Hu, LK Grunenfelder, T Centea, S. Nutt, In situ monitoring and analysis of void evolution in unidirectional prepreg, J. Compos. Mater. 52 (2018) 2847–2858, doi:10.1177/0021998318759183.

[12] A Hautefeuille, S Comas-Cardona, C. Binetruy, Mechanical signature and full-field measurement of flow-induced large in-plane deformation of fibrous reinforcements in composite processing, Appl. Sci. Manufact. 118 (2019) 213–222, doi:10.1016/j.compositesa.2018.12.030.

[13] L Salvo, M Suéry, A Marmottant, N Limodin, D. Bernard, 3D imaging in material science: Application of X-ray tomography, Comptes Rendus Physique 11 (2010) 641–649, doi:10.1016/j.crhy.2010.12.003.

[14] SC Garcea, Y Wang, PJ. Withers, X-ray computed tomography of polymer composites, Compos. Sci. Technol. 156 (2018) 305–319, doi:10.1016/j.compscitech.2017.10.023.

[15] T Centea, P. Hubert, Measuring the impregnation of an out-of-autoclave prepreg by micro-CT, Compos. Sci. Technol. 71 (2011) 593–599, doi:10.1016/j.compscitech.2010.12.009.

[16]

T Centea, G Peters, K Hendrie, S. Nutt, Effects of thermal gradients on defect formation during the consolidation of partially impregnated prepregs, J. Compos. Mater. 51 (2017) 3987–4003, doi:10.1177/0021998317733317.

[17] JJ Torres, M Simmons, F Sket, C. González, An analysis of void formation mechanisms in out-of-autoclave prepregs by means of X-ray computed tomography, Appl. Sci. Manufact. 117 (2019) 230–242, doi:10.1016/j.compositesa.2018.11.010.

[18] S Schleef, H Löwe, M. Schneebeli, Hot-pressure sintering of low-density snow analyzed by X-ray microtomography and in situ microcompression, Acta Mater. 71 (2014) 185–194, doi:10.1016/j.actamat.2014.03.004.

[19] NM Larson, FW. Zok, In-situ 3D visualization of composite microstructure during polymer-to-ceramic conversion, Acta Mater. 144 (2018) 579–589, doi:10.1016/j.actamat.2017.10.054.

[20] R Zhu, G Niu, Z Qu, P Wang, R Zhang, D. Fang, In-situ quantitative tracking of micro-crack evolution behavior inside CMCs under load at high temperature: A deep learning method, Acta Mater. 255 (2023) 119073, doi:10.1016/j.actamat.2023.119073.

[21] J Dewanckele, MA Boone, F Coppens, D Van Loo, AP. Merkle, Innovations in laboratory-based dynamic micro-CT to accelerate in situ research, J. Microsc. 277 (2020) 197–209, doi:10.1111/jmi.12879.

[22] J Kratz, P Galvez-Hernandez, LR Pickard, J Belnoue, K. Potter, Lab-based in-situ micro-CT observation of gaps in prepreg laminates during consolidation and cure, Composites Part A: (2021), doi:10.1016/j.compositesa.2020.106180.

[23] Galvez-Hernandez P, Jimenez-Martin C, Smith R, Maes V, McMahon T, Sinclair I. In-situ CT of out-of-autoclave composites manufacturing processes. Proceedings of the international conference on manufacturing of advanced composites 2022 (ICMAC), Sheffield, UK: 2022.

[24] T-H Le, PJJ Dumont, L Orgéas, D Favier, L Salvo, E. Boller, X-ray phase contrast microtomography for the analysis of the fibrous microstructure of SMC composites, Appl. Sci. Manufact. 39 (2008) 91–103, doi:10.1016/j.compositesa.2007.08.027.

[25] J Vilà, F Sket, F Wilde, G Requena, C González, J. LLorca, An in situ investigation of microscopic infusion and void transport during vacuum-assisted infiltration by means of X-ray computed tomography, Compos. Sci. Technol. 119 (2015) 12–19, doi:10.1016/j.compscitech.2015.09.016.

[26] D Ferré Sentis, L Orgéas, PJJ Dumont, S Rolland du Roscoat, M Sager, P Latil, 3D in situ observations of the compressibility and pore transport in Sheet Moulding Compounds during the early stages of compression moulding, Appl. Sci. Manufact. 92 (2017) 51–61, doi:10.1016/j.compositesa.2016.10.031.

[27] NM Larson, FW. Zok, Insights from in-situ X-ray computed tomography during axial impregnation of unidirectional fiber beds, Appl. Sci. Manufact. 107 (2018) 124–134, doi:10.1016/j.compositesa.2017.12.024.

[28] B de Parscau du Plessix, P Lefébure, N Boyard, SL Corre, N Lefèvre, F Jacquemin, et al., In situ real-time 3D observation of porosity growth during composite part curing by ultra-fast synchrotron X-ray microtomography, J. Compos. Mater. 53 (2019) 4105–4116, doi:10.1177/0021998319846260.

[29] Y Lakroune, L Orgéas, P Dumont, F Martoïa, SRD Roscoat, F Jacquemin, et al., Analyse 3D en temps réel et in situ des mécanismes de (dé)consolidation dans les composites thermoplastiques

renforcés lors de leur thermo-estampage, Ecole Nationale Supérieure d'Arts et Métiers (ENSAM) Bordeaux, Talence, France, 2019, p. 7.

[30] NM Larson, C Cuellar, FW. Zok, X-ray computed tomography of microstructure evolution during matrix impregnation and curing in unidirectional fiber beds, Appl. Sci. Manufact. 117 (2019) 243–259, doi:10.1016/j.compositesa.2018.11.021.

[31] L Amedewovo, L Orgéas, B de Parscau du Plessix, N Lefevre, A Levy, S Le Corre, Deconsolidation of carbon fiber-reinforced PEKK laminates: 3D real-time in situ observation with synchrotron X-ray microtomography, Appl. Sci. Manufact. 177 (2024) 107917, doi:10.1016/j.compositesa.2023.107917.

[32] G Niu, R Zhu, H Lei, R Zhang, P Wang, Z Qu, et al., Internal damage evolution investigation of C/SiC composites using in-situ tensile X-ray computed tomography testing and digital volume correlation at 1000°C, Appl. Sci. Manufact. 163 (2022) 107247, doi:10.1016/j.compositesa.2022.107247.

[33] T Chatziathanasiou, J Soete, J Vanhulst, D Carrella-Payan, L Gorbatikh, M. Mehdikhani, In-situ X-ray computed tomography of mode I delamination in carbon-epoxy composites: The effect of the interface ply orientation, Engineering 260 (2023) 110761, doi:10.1016/j.compositesb.2023.110761.

[34] NE Deresse, C Van Steen, J Soete, M Sarem, J vanhulst, M Wevers, et al., Fracture mode analysis of cementitious mortars by simultaneous application of 4D-XCT and acoustic emission technique, Constr. Build. Mater. 419 (2024) 135486, doi:10.1016/j.conbuildmat.2024.135486.

[35] A Piovesan, R Nicasy, T Arens, B Dequeker, J Soete, C Achille, et al., Multiscale modelling of capillary imbibition in 3D-printed porous microfluidic channels, Microfluid Nanofluid 26 (2022) 21, doi:10.1007/s10404-022-02528-0.

[36] L Snels, N Mostofi Sarkari, J Soete, A Maes, C Antonini, M Wevers, et al., Internal and interfacial microstructure characterization of ice droplets on surfaces by X-ray computed tomography, J. Colloid. Interface Sci. 637 (2023) 500–512, doi:10.1016/j.jcis.2023.01.103.

[37] N Lu, S Moniri, MR Wiltse, J Spielman, N Senabulya, AJ. Shahani, Dynamics of Ga penetration in textured Al polycrystal revealed through multimodal three-dimensional analysis, Acta Mater. 217 (2021) 117145, doi:10.1016/j.actamat.2021.117145.

[38] Gayot SF, Soete J, Vanhulst J, Bailly C, Gérard P, Pardoen T. Monitoring void formation during liquid composite molding by in-situ x-ray computed tomography. Proceedings of the 37th ASC Annual Technical Conference, Tucson, Arizona, USA: 2022.

[39] J Hemmer, AS Dharmalingam, A-S Lectez, C Burtin, S Comas-Cardona, C Binetruy, et al., Compaction behaviour of tow at meso-scale: experimental investigations of morphological evolution at dry, lubricated and saturated states, Mater. Sci. Eng. 406 (2018) 012020, doi:10.1088/1757-899X/406/1/012020.

[40] J Hemmer, C Burtin, S Comas-Cardona, C Binetruy, T Savart, A. Babeau, Unloading during the infusion process: direct measurement of the dual-scale fibrous microstructure evolution with X-ray computed tomography, Appl. Sci. Manufact. 115 (2018) 147–156, doi:10.1016/j.compositesa.2018.09.013.

[41] Q. Charlier, Adhesion phenomena in thermoplastic composites based on acrylic matrices obtained by free radical polymerization, Institut National des Sciences Appliquées de Lyon, 2015.

[42] DS. Cousins, Advanced thermoplastic composites for wind turbine blade manufacturing, Colorado School Mines (2018).

[43] SF Gayot, C Bailly, T Pardoen, P Gérard, F. Van Loock, Processing maps based on polymerization modelling of thick methacrylic laminates, Mater. Des. 196 (2020) 109170, doi:10.1016/j.matdes.2020.109170.

[44] B Palmieri, A Petriccione, G De Tommaso, M Giordano, A. Martone, An efficient thermal cure profile for thick parts made by reactive processing of acrylic thermoplastic composites, J. Compos. Sci. 5 (2021) 229, doi:10.3390/jcs5090229.

[45] SF Gayot, C Bailly, T Pardoen, P. Gérard, Relationship between processing parameters and mechanical properties of thick glass fibre reinforced thermoplastic methacrylic composites, in: A. Turon, P. Maimí, M. Fagerström (Eds.), Proceedings of the 7th ECCOMAS Thematic Conference on the Mechanical Response of Composites, Girona, Spain, 2019.

[46] CA Schneider, WS Rasband, KW. Eliceiri, NIH Image to ImageJ: 25 years of image analysis, Nat. Methods 9 (2012) 671–675, doi:10.1038/nmeth.2089.

[47] Y De Parseval, KM Pillai, SG. Advani, A simple model for the variation of permeability due to partial saturation in dual scale porous media, Transp. Porous. Media 27 (1997) 243–264.

[48] Grimsley BW, Hubert P, Song X, Cano RJ, Loos AC, Pipes RB. Flow and compaction during the vacuum assisted resin transfer molding process. Proceedings of 33rd ISTC, Seattle, WA (USA): 2001, p. 1–14.

[49] M Moghaddam, A Breede, C Brauner, W. Lang, Embedding piezoresistive pressure sensors to obtain online pressure profiles inside fiber composite laminates, Sensors 15 (2015) 7499–7511, doi:10.3390/s150407499.

[50] Hemmer J. Rapport intermédiaire d'expériences 2016.

[51] Odian GG. Principles of polymerization. 4th ed. Hoboken, NJ (USA): Wiley-Interscience; 2004.

[52] K Yamada, H Emori, K. Nakazawa, Time-evolution of bubble formation in a viscous liquid, Earth Planet Sp. 60 (2008) 661–679, doi:10.1186/BF03353130.

Graphical abstract

Images may appear blurred during proofing as they have been optimized for fast web viewing. A high quality version will be used in the final publication. Click on the image to view the original version.

alt-text: Image, graphical abstract

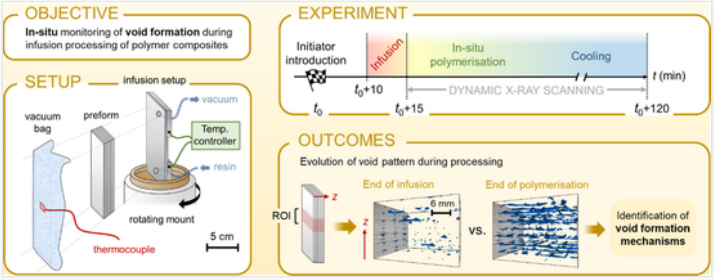

Queries and Answers

Q1

Query: Please review the given names (no colouring) and surnames (highlighted in teal colouring) to make sure that we have identified them correctly and that they are presented in the desired order. Carefully verify the spelling of all authors' names as well. If changes are needed, please provide the edits in the author section.

Answer: Yes

Q2

Query: Your article is registered as a regular item and is being processed for inclusion in a regular issue of the journal. If this is NOT correct and your article belongs to a Special Issue/Collection please contact k.ku@elsevier.com immediately prior to returning your corrections.

Answer: This is correct